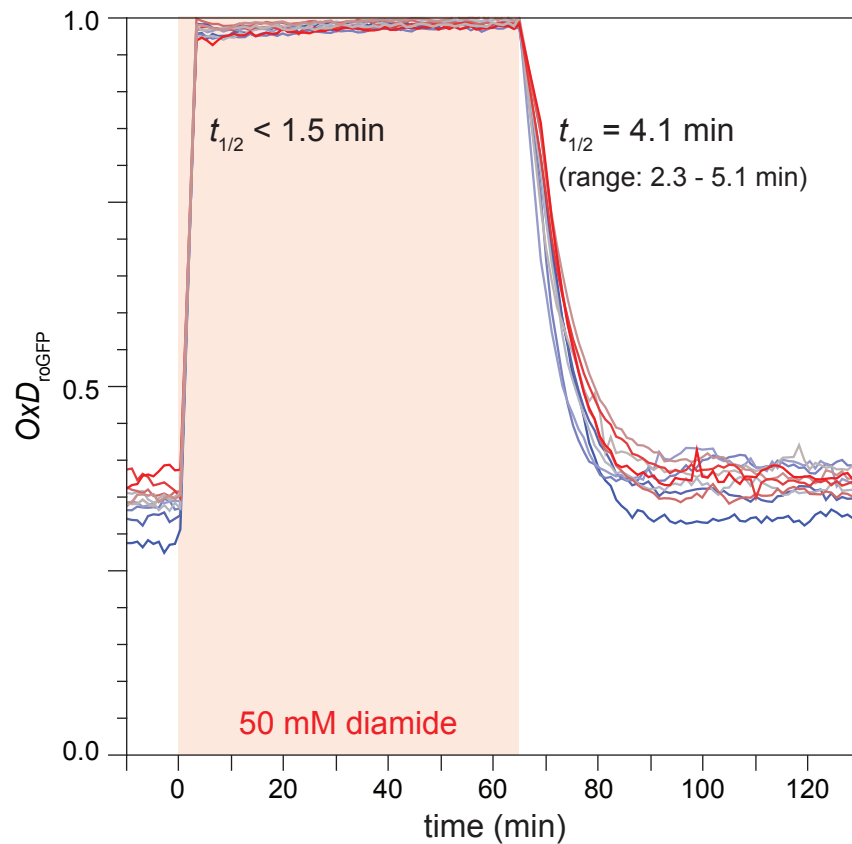# Supplementary Information:

Regulated spatial organization and sensitivity of cytosolic protein oxidation in *Caenorhabditis elegans*

Catalina Romero-Aristizabal, Debora S. Marks, Walter Fontana, Javier Apfeld

Supplementary Figure 1: *In vivo* **kinetics of roGFP1_R12 oxidation and recovery.**

To determine the sensor's kinetics in response to oxidation (diamide) and recovery from that treatment, we acquired OxD_{roGFP} time courses from the pm3 muscles of 10 animals imaged for 10 minutes before treatment, shifted to 50 mM diamide for 60 minutes (oxidation phase; red background), and then shifted back to normal conditions for an additional 60 minutes (recovery phase). Images were acquired once a minute, with a 3 (4) minute operational gap when an animal was first exposed to (or removed from) diamide. Each animal's OxD_{roGFP} time course is colored by the average value of OxD_{roGFP} (baseline) before diamide treatment. The average time for a half-maximal response ($t_{1/2}$) is less than 1.5 minutes for exposure to oxidant and 4.1 minutes for recovery from oxidant.
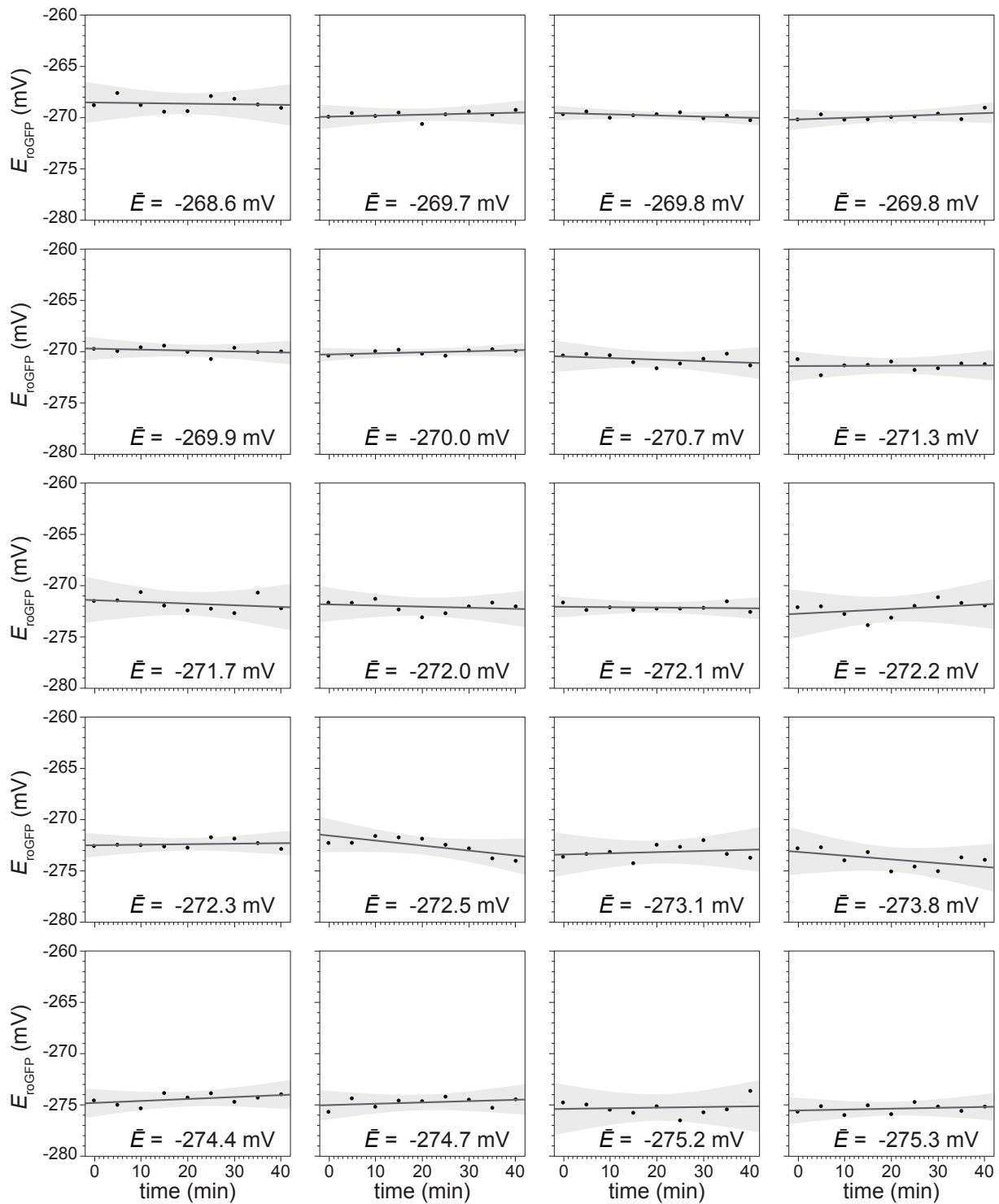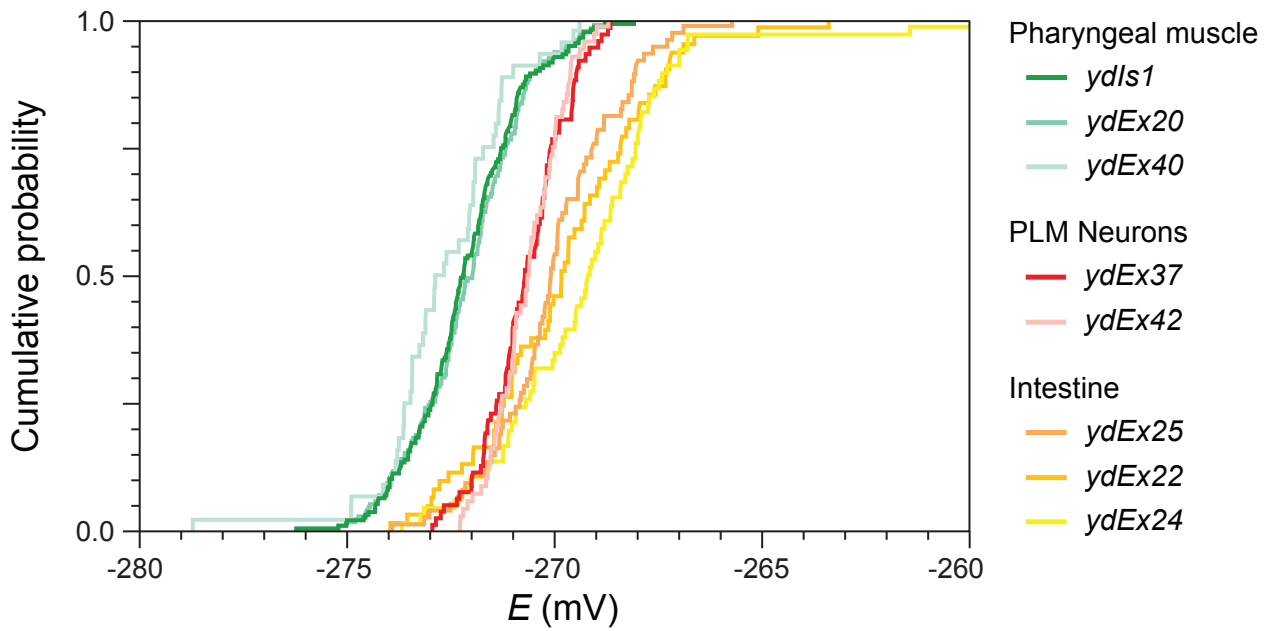
Supplementary Figure 2: roGFP1_R12 redox potentail is stable over time.

Time-course measurements of E_{roGFP} in the pharyngeal muscles in 20 untreated animals. Linear regression fits are shown as solid lines flanked by shaded grey areas marking the Bonferroni-corrected 95% confidence interval of the fit. No significant time-dependence was observed for any of the time courses ($p > 0.05$ in all cases). Images were acquired every 5 minutes for 40 minutes.
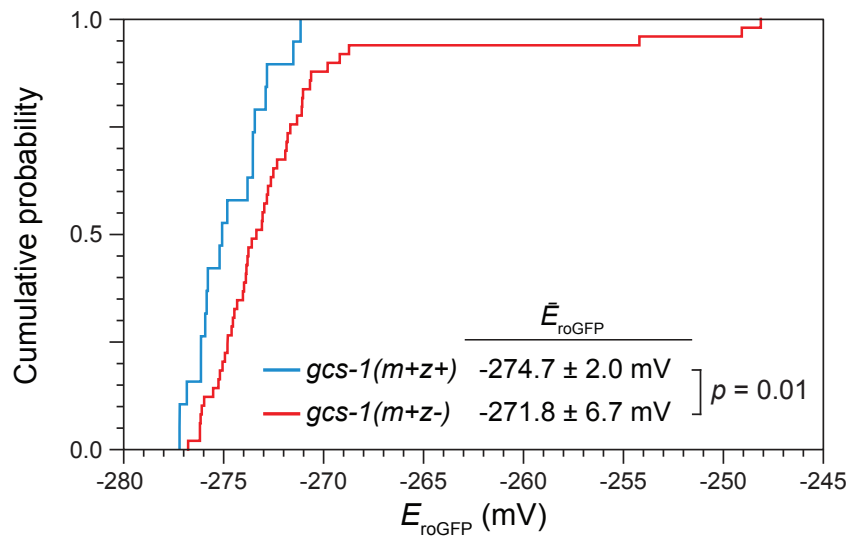
Supplementary Figure 3: roGFP1_R12 responds to changes in glutathione synthesis.

Cumulative distributions of the sensor's redox potential in the cytosol of feeding muscles in *gcs-1(maternal+ zygotic-)* animals (red, 49 animals) and their *gcs-1(maternal+ zygotic+)* siblings (blue, 19 animals). The inset table shows the mean E_{roGFP} values of each group ± one standard error of the mean. Differences in average potential between these two groups were significant ($p = 0.01$, Wilcoxon Exact test).

Supplementary Figure 4: Tissue-specific differences in the sensor's redox potential in multiple roGFP1_R12 transgenic lines.

Cumulative distributions of the sensor's redox potential in multiple transgenic lines expressing the roGFP1_R12 sensor in the cytosol of pharyngeal muscles (green lines), PLM touch neurons (red lines), and intestine (orange lines). The average redox potentials and population sizes (in parenthesis) were: -272.1 mV (185), -272.0 mV (170), and -272.6 mV (44), respectively, for the *ydIs1*, *ydEx20*, and *ydEx40* pharyngeal muscle lines; -270.7 mV (78) and -270.6 mV (68) for the *ydEx35*, and *ydEx42* PLM neuronal lines; and -270.0 mV (74), -269.8 mV (61), and -269.2 mV (66), respectively, for the *ydEx25*, *ydEx22*, and *ydEx24* intestinal lines. All transgenic lines were generated independently, except for *ydIs1*, which was derived by chromosomal integration of *ydEx20*. Differences in average potential between tissues were significant ($p < 0.05$ for all pair-wise comparisons between lines of different tissues, Tukey HSD test). No statistical difference in redox potential was observed between lines expressing the sensor in the same tissue ($p > 0.05$ for all pair-wise comparisons, Tukey HSD test).
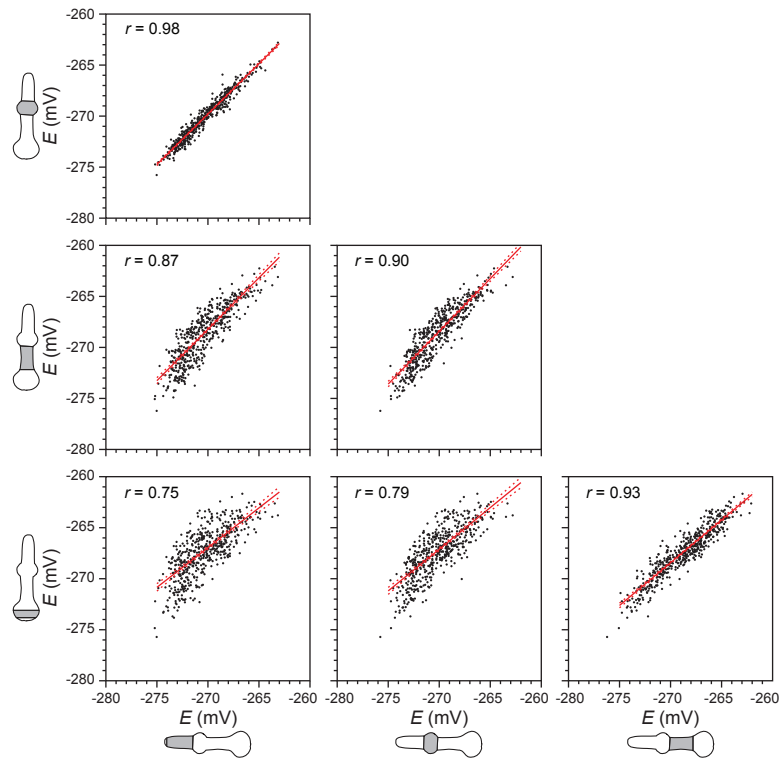
Supplementary Figure 5: E_{roGFP} varies in a concerted manner throughout the pharynx.

Scatter-plots of E_{roGFP} values in pm3, pm5 and pm7 for the 394 wild-type individuals in Fig. 3 are arranged in a matrix. The pharynx-shaped logos denote the segments to which the redox potential values refer. Linear regression fits are shown as solid lines flanked by dashed lines marking the 95% confidence interval of the fit. The regression line is red if $p < 0.0001$ for the correlation coefficient r.
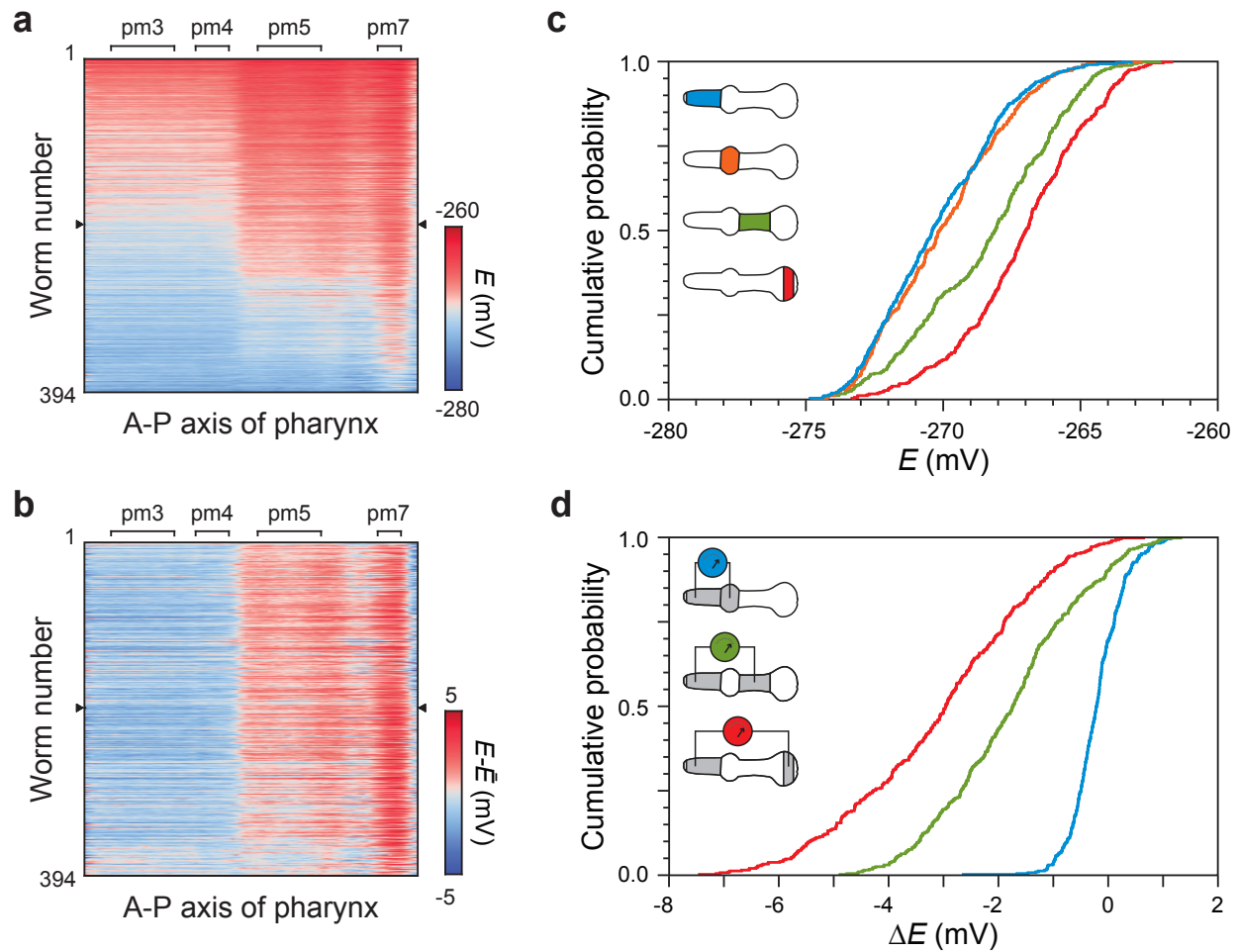
Supplementary Figure 6: E_{roGFP} regions align sharply with muscle boundaries.

(**a**) Each of the 394 horizontal lines represents the sensor's redox profile along the anterior-posterior axis of the pharynx of a wild type individual. The profiles are sorted by decreasing average potential. Figure 3b gives a functional representation of these profiles. The black arrows on the margins indicate the individual shown in Fig. 3a.

(**b**) This panel results from subtracting the average sensor's redox potential of an individual from its profile in panel a. Arrows indicate the individual in Fig. 3a.

(**c**) Cumulative distributions of sensor's redox potentials for the four muscle segments pm3, pm4, pm5, and pm7. For statistics see Supplementary Table 2a.

(**d**) Cumulative distributions of the difference in redox potential between pairs of muscle segments. For statistics see Supplementary Table 2b.
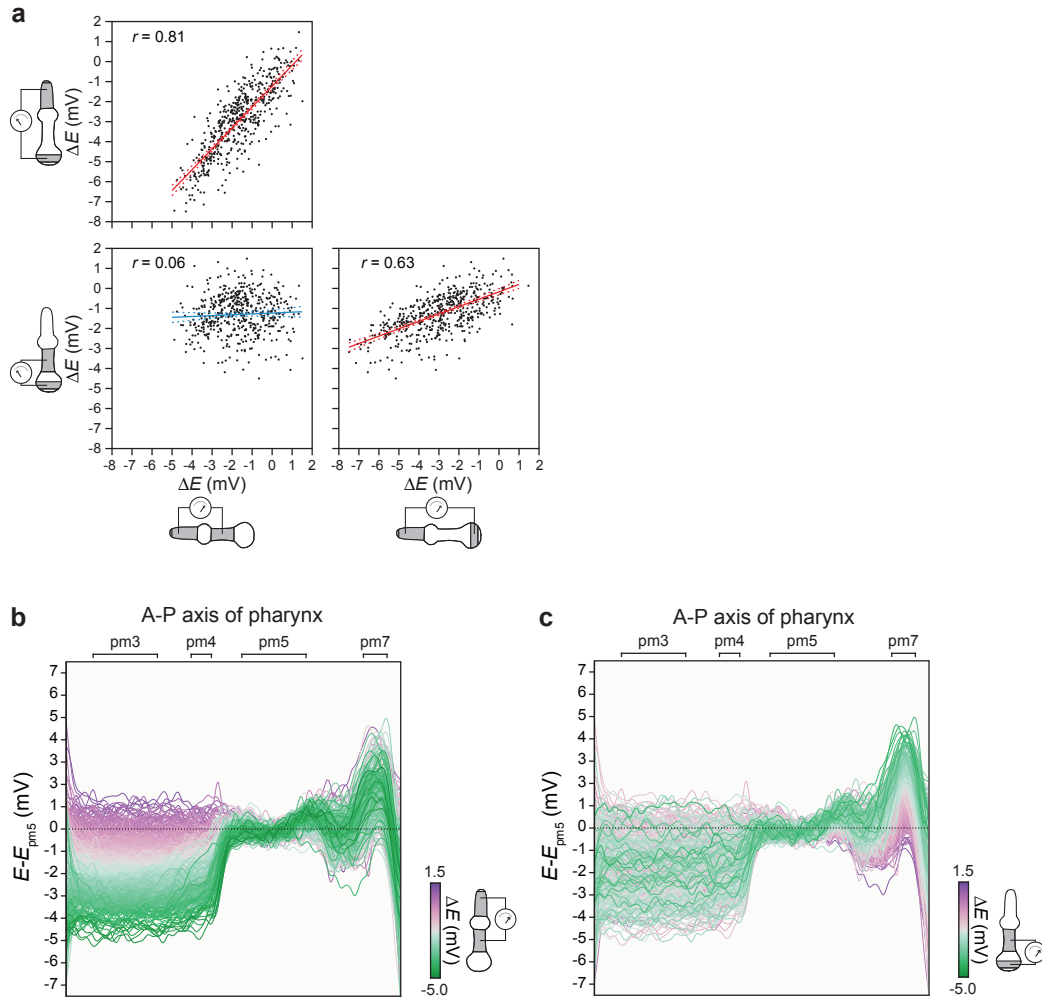
Supplementary Figure 7: Independent mechanisms generate the spatial redox pattern.

(**a**) Scatter-plots of *ΔE* values between pairs of pharyngeal segments are arranged in a matrix. The pharynx-shaped logos denote the segments to which the redox differences refer. Linear regression fits are shown as solid lines flanked by dashed lines marking the 95% confidence interval of the fit. The regression line is red if $p < 0.0001$ and blue if $p > 0.05$ for the correlation coefficient r. Separate mechanisms specify the sensor's redox potential in pm3 and pm7 muscles, since differences in potential between pm3 and pm5 muscles are uncorrelated with differences in potential between pm5 and pm7 muscles.

(**b-c**) These panels depict the pharyngeal redox potentials E_{roGFP} along the anterior-posterior axis for each of the 394 wild-type animals shown in Fig. 3b. Each profile is the best-fit functional (*i.e.* continuous) representation of the observed E_{roGFP} values using a B-spline basis (see Supplementary Methods). In both panels these profiles are registered on pm5, that is, we subtract from each profile the average potential in its pm5 region. In panel b, profiles are colored based on their redox-potential difference between pm3 and pm5 muscles; in panel c, they are colored based on their difference between pm5 and pm7 muscles. The lack of correlation between these two differences (panel a) is evidenced by the random mixing of profiles in the pm7 segment in panel b and the pm3 and pm4 segments in panel c.
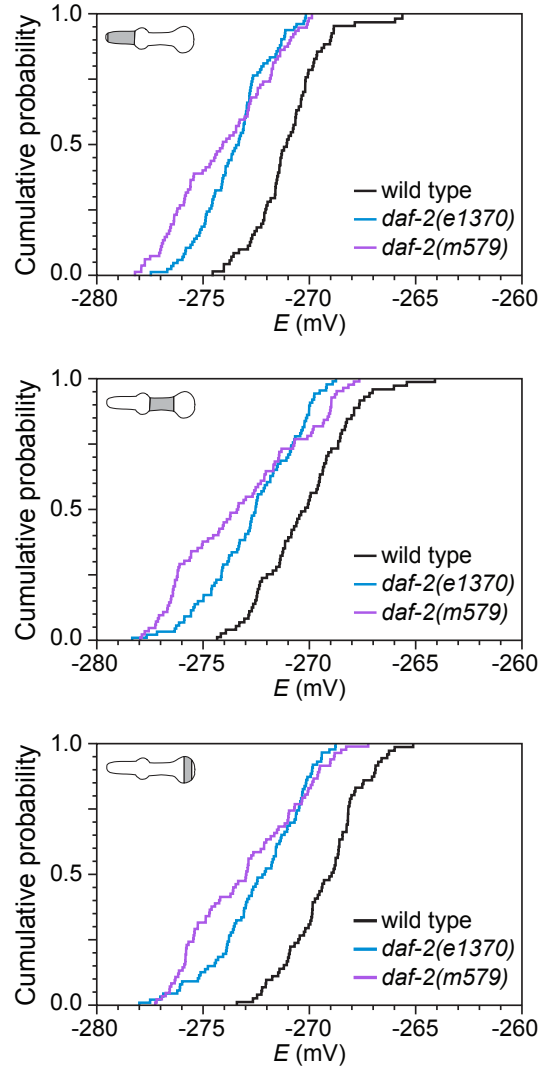
Supplementary Figure 8: Loss-of-function mutations in the insulin receptor gene *daf-2* lower the sensor's redox potential in the pharynx.

The *e1370* allele contains a point mutation affecting the DAF-2 kinase domain[1] and leads to a strong loss of function. The *m579* allele contains a point mutation in the ligand binding domain that causes type A insulin resistance in humans[2, 3]. Both *daf-2* alleles exhibit lower values of the sensor's redox potential in feeding muscles than wild-type animals. For statistics see Supplementary Table 3b.
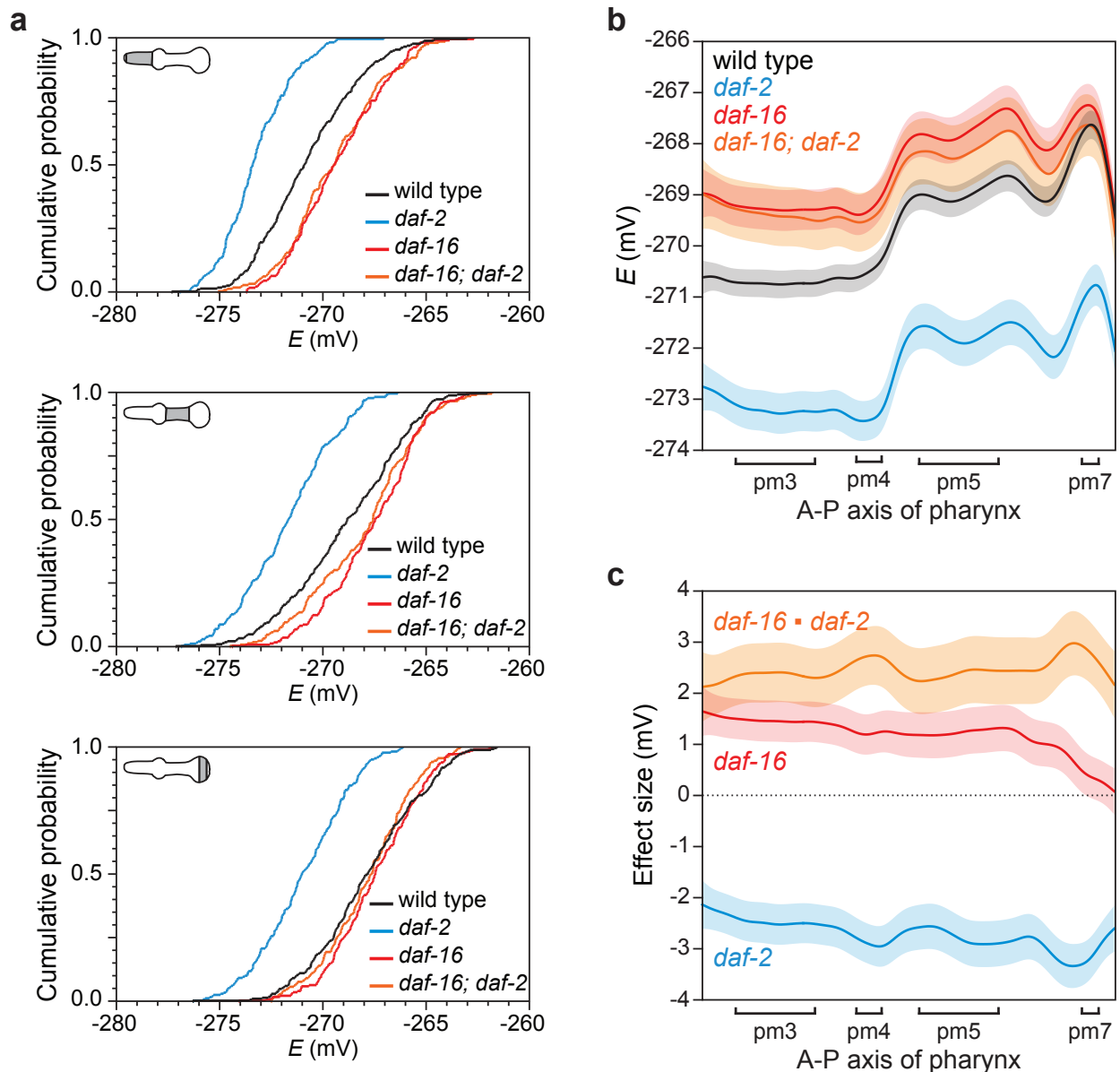
Supplementary Figure 9: Insulin signaling regulates the spatial redox pattern of the pharynx.

(**a**) The effects of insulin signaling on the sensor's redox potential for each pharyngeal region are shown as cumulative distributions. Compared to wild type (black), *daf-16 (mu86)* mutants (red) have a higher potential in pm3 (top) and pm5 (middle), but not in pm7 (bottom). Compared to wild type, *daf-2(e1370)* mutants (blue) have a lower potential in all muscles. The *daf-16(mu86); daf-2(e1370)* double mutant (orange) shows that redox regulation through signaling by DAF-2 depends on DAF-16. For statistics see Supplementary Table 3c.

(**b**) This panel shows the reconstructed average pharyngeal redox profiles of wild type and mutant genotypes, derived using functional regression (as detailed in panel c). Black: wild type; blue: *daf-2(e1370)*; red: *daf-16(mu86)*; orange: *daf-16(mu86); daf-2(e1370)*.

(**c**) The anterior-posterior redox profile E of each individual can be expressed as the wild type re-dox profile *wt* plus effect terms from the categorical variables *daf-2*, *daf-16*, and an interaction term *daf-2 ◊ daf- 16*: $E = wt + daf\text{-}2 + daf\text{-}16 + daf\text{-}2 ◊ daf\text{-}16 + error$. This procedure yields position-de-pendent terms that quantify the effects of *daf-16(mu86)* and *daf-2(e1370)* backgrounds (red and blue, respectively) as well as of their genetic interaction (orange) relative to wild type. From these terms we can reconstruct the average redox profile of each genotype, shown in panel c, as follows. Wild type: $E = wt$; *daf-16(mu86)* mutant: $E = wt + daf\text{-}16$; *daf-2(e1370)* mutant: $E = wt + daf\text{-}2$; and *daf-16(mu86); daf-2(e1370)* double mutant: $E = wt + daf\text{-}2 + daf\text{-}16 + daf\text{-}2 ◊ daf\text{-}16$. Shaded areas represent 95% point-wise confidence intervals.
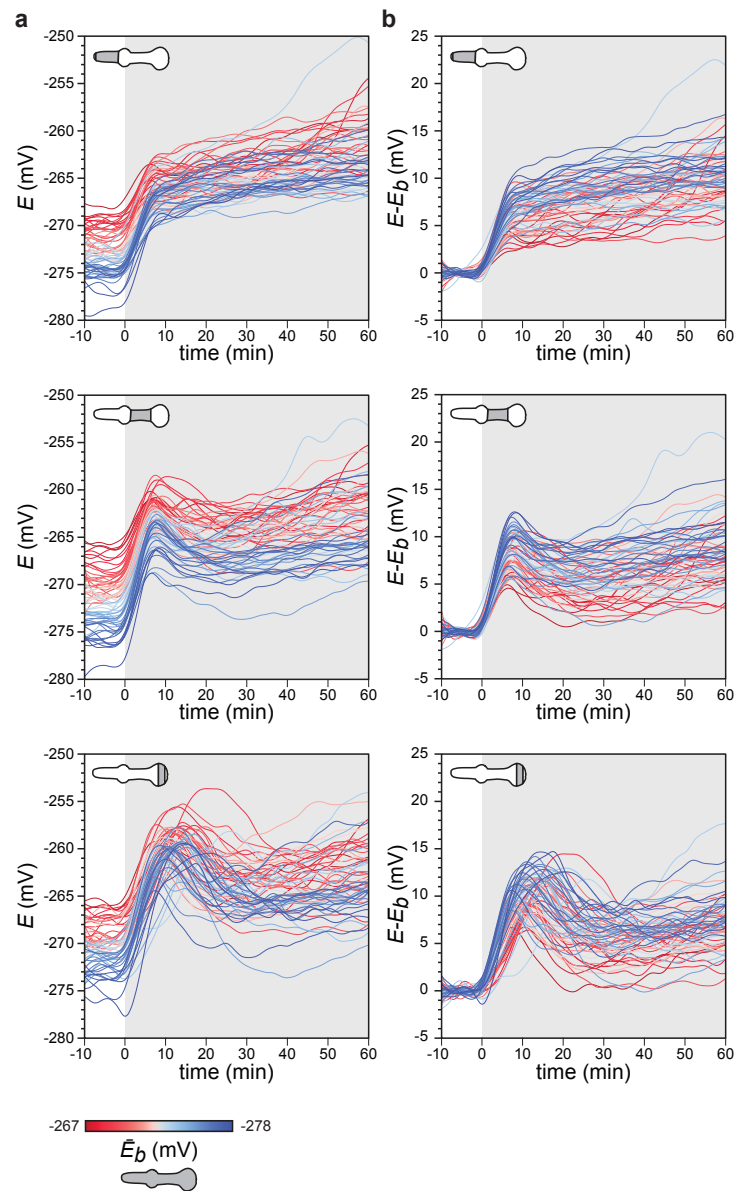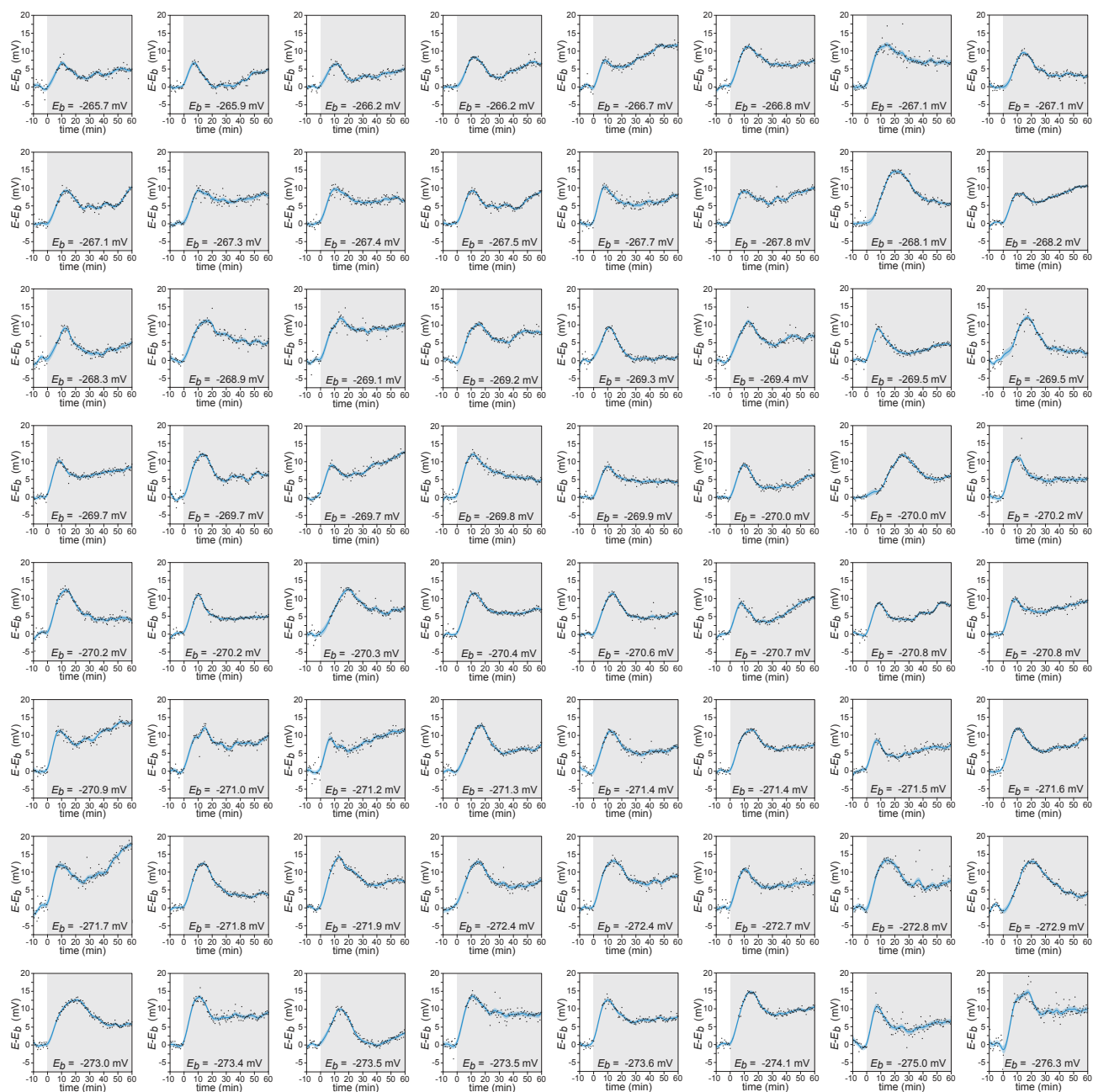
Supplementary Figure 10: Redox dynamics in response to oxidant treatment.

We acquired individual redox time courses in pm3, pm5 and pm7 of 64 animals before and after oxidant treatment. Individuals were observed in the absence of treatment for 10 minutes and subsequently treated with 5 mM *tert*-butyl hydroperoxide (*t*-BuOOH) for 60 minutes. Images were acquired every 30 seconds with a 6 minute gap between treatment conditions.

(**a**) The panels show the dynamics of the sensor's redox potential in three pharyngeal segments after converting the data into a functional representation $E(t)$ using a B-spline basis (see Supplementary Methods). Trajectories are colored based on the average value of the redox potential of the whole tissue in the interval prior to oxidant treatment ($\bar{E}_b$). Thus, each animal is assigned the same color in all panels.

(**b**) Same as panel a but showing the trajectories of each pharyngeal segment corrected by their respec-

tive baselines, $E(t) - E_b$.

Supplementary Figure 11: Redox dynamics in response to oxidant treatment in pm7 muscles.

The observed redox potential values of 64 animals were baseline corrected (black dots) and threaded into a continuous trace (blue line) using a B-spline basis (see Supplementary Methods). The shaded blue area represents the point-wise 95% confidence interval for the fit. Exposure to 5 mM t-BuOOH starts at time zero. The collection of graphs, sorted by E_b, serves the purpose of conveying the faithful representation achieved by functionalizing the data points.

Supplementary Table 1: Statistical analysis of cytosolic redox potentials of different tissues.

Descriptive statistics

Genotype	Tissue	E [mean ± s.d. (n), mV]
wild type	pharynx	-270.9 ± 1.7 (276)
	intestine	-268.1 ± 2.1 (276)
	PLM neurons	-269.9 ± 1.3 (239)
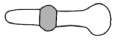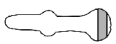
Statistical comparisons between tissues

Genotype	Tissues		$\Delta\langle E\rangle$ [mean ± s.e., mV]	p-value
wild type	intestine	pharynx	2.8 ± 0.1	< 0.0001
	intestine	PLM neurons	1.7 ± 0.2	< 0.0001
	PLM neurons	pharynx	1.1 ± 0.2	< 0.0001
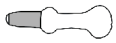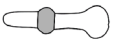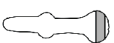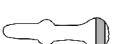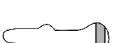
Supplementary Table 2: Statistical analysis of redox potentials in pharyngeal muscle segments.

a) Cytosolic redox potentials of pharyngeal muscle segments

Descriptive statistics

Genotype	Muscle segment	E [mean ± s.d. (n), mV]
	[segment 1 diagram]	-270.2 ± 2.3 (394)
	[segment 2 diagram]	-270.0 ± 2.3 (394)
wild type	[segment 3 diagram]	-268.4 ± 2.6 (394)
	[segment 4 diagram]	-267.1 ± 2.4 (394)

Statistical comparisons between muscle segments

Genotype	Muscle segments		$\Delta\langle E\rangle$ [mean ± s.e., mV]	p-value
	[segment 1 diagram]	[segment 2 diagram]	-0.2 ± 0.2	0.6409
	[segment 1 diagram]	[segment 3 diagram]	-1.8 ± 0.2	< 0.0001
	[segment 1 diagram]	[segment 4 diagram]	-3.1 ± 0.2	< 0.0001
wild type	[segment 2 diagram]	[segment 3 diagram]	-1.6 ± 0.2	< 0.0001
	[segment 2 diagram]	[segment 4 diagram]	-2.9 ± 0.2	< 0.0001
	[segment 3 diagram]	[segment 4 diagram]	-1.3 ± 0.2	< 0.0001

b) Cytosolic redox-potential differences between pharyngeal muscle segments within individuals

Descriptive statistics

Genotype	Muscle segment pair	ΔE [mean ± s.d. (n), mV]
wild type		-0.2 ± 0.5 (394)
		-1.8 ± 1.3 (394)
		-3.1 ± 1.6 (394)
		-1.6 ± 1.1 (394)
		-2.9 ± 1.5 (394)
		-1.3 ± 1.0 (394)

Statistical comparisons between muscle segment pairs

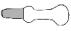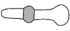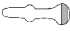| Genotype	Muscle segment pairs		$\Delta\langle\Delta E\rangle$ [mean ± s.e., mV]	p-value
wild type			-1.6 ± 0.1	<0.0001
			-2.9 ± 0.1	<0.0001
			-1.4 ± 0.1	<0.0001
			-2.7 ± 0.1	<0.0001
			-1.1 ± 0.1	<0.0001
			-1.3 ± 0.1	<0.0001
			-1.1 ± 0.1	<0.0001
			-0.2 ± 0.1	0.1915
			-1.5 ± 0.1	<0.0001
			-1.3 ± 0.1	<0.0001
			-0.2 ± 0.1	0.1915
			-0.5 ± 0.1	<0.0001
			-1.8 ± 0.1	<0.0001
			-0.3 ± 0.1	0.0223
			-1.6 ± 0.1	<0.0001

Supplementary Table 3: Statistical analysis of insulin signaling's effect on cytosolic redox potential.

a) Effect of *daf-2(e1370)* on the cytosolic redox potentials of different tissues
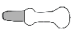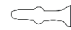
Tissue	Genotype	E [mean ± s.d. (n), mV]	$\Delta\langle E\rangle$ [mean ± s.e., mV]	p-value
Pharynx	wild type	-270.4 ± 1.8 (227)	-2.2 ± 0.2	< 0.0001
	daf-2(e1370)	-272.6 ± 1.8 (263)		
Intestine	wild type	-268.1 ± 2.1 (276)	-3.2 ± 0.2	< 0.0001
	daf-2(e1370)	-271.3 ± 1.8 (151)		
PLM neurons	wild type	-269.8 ± 0.9 (133)	0.1 ± 0.1	0.7
	daf-2(e1370)	-269.8 ± 1.0 (205)		

b) Effect of *daf-2* alleles *e1370* and *m579* on the cytosolic redox potentials of pharyngeal muscle segments

Descriptive statistics
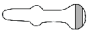
Genotype	E [mean ± s.d. (n), mV]	E [mean ± s.d. (n), mV]	E [mean ± s.d. (n), mV]	E [mean ± s.d. (n), mV]
wild type	-271.0 ± 1.7 (71)	-271.0 ± 1.7 (71)	-270.2 ± 2.1 (71)	-269.3 ± 1.8 (71)
daf-2(m579)	-274.1 ± 2.3 (82)	-274.4 ± 2.7 (82)	-273.3 ± 3.0 (82)	-273.0 ± 2.7 (82)
daf-2(e1370)	-273.5 ± 1.6 (86)	-274.0 ± 1.9 (86)	-272.6 ± 2.2 (86)	-272.4 ± 2.2 (86)

Statistical comparisons between genotypes

Genotype pair		Statistic				
wild type	*daf-2(m579)*	$\Delta\langle E\rangle$ [mean ± s.e., mV]	-3.0 ± 0.3	-3.4 ± 0.4	-3.0 ± 0.4	-3.8 ± 0.4
		p-value	< 0.0001	< 0.0001	< 0.0001	< 0.0001
wild type	*daf-2(e1370)*	$\Delta\langle E\rangle$ [mean ± s.e., mV]	-2.5 ± 0.3	-3.0 ± 0.3	-2.4 ± 0.4	-3.1 ± 0.4
		p-value	< 0.0001	< 0.0001	< 0.0001	< 0.0001
daf-2(m579)	*daf-2(e1370)*	$\Delta\langle E\rangle$ [mean ± s.e., mV]	-0.5 ± 0.3	-0.4 ± 0.3	-0.6 ± 0.4	-0.6 ± 0.3
		p-value	0.161	0.395	0.247	0.157
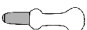
c) Effect of insulin signaling on the redox potentials of pharyngeal muscle segments

Descriptive statistics

Genotype	E [mean ± s.d. (n), mV]	E [mean ± s.d. (n), mV]	E [mean ± s.d. (n), mV]	E [mean ± s.d. (n), mV]
wild type	-270.8 ± 2.4 (273)	-270.2 ± 2.5 (273)	-268.9 ± 2.8 (273)	-267.9 ± 2.6 (273)
daf-2(e1370)	-273.2 ± 1.7 (225)	-273.1 ± 1.8 (225)	-271.7 ± 2.2 (225)	-271.0 ± 2.2 (225)
daf-16(mu86)	-269.4 ± 2.2 (224)	-269.0 ± 2.2 (224)	-267.7 ± 2.3 (224)	-267.5 ± 2.2 (224)
daf-16(mu86); daf-2(e1370)	-269.5 ± 2.4 (209)	-269.2 ± 2.4 (209)	-268.1 ± 2.6 (209)	-267.8 ± 2.1 (209)

Parameter estimates for linear models of each muscle segment

Model: E = Intercept + *daf-2* + *daf-16* + *daf-2* * *daf-16* + ε

Term					
Intercept	Estimate ± s.e. (mV)	-270.8 ± 0.1	-270.2 ± 0.1	-268.9 ± 0.2	-267.9 ± 0.1
	p-value	< 0.0001	< 0.0001	< 0.0001	< 0.0001
daf-2	Estimate ± s.e. (mV)	-2.5 ± 0.2	-2.8 ± 0.2	-2.8 ± 0.2	-3.1 ± 0.2
	p-value	< 0.0001	< 0.0001	< 0.0001	< 0.0001
daf-16	Estimate ± s.e. (mV)	1.4 ± 0.2	1.3 ± 0.2	1.2 ± 0.2	0.4 ± 0.2
	p-value	< 0.0001	< 0.0001	< 0.0001	0.0555
daf-2 * daf-16	Estimate ± s.e. (mV)	2.4 ± 0.3	2.6 ± 0.3	2.4 ± 0.3	2.7 ± 0.3
	p-value	< 0.0001	< 0.0001	< 0.0001	< 0.0001

Supplementary Table 4: Primers.

Primer	Sequence
WF38	GGCTGAAATCACTCACAACG
WF45	GAGTCAGTGAGCGAGGAAGC
WF46	TTCTTCTCCTTTACTCATTTTTTCTACCGGTACCCTCCTGAAAATGTTCTATGTTATGTT
WF49	CTTTACTCATTTTTTCTACCGGTACCAATACGACTCACTATAGGGCACCC
WF96	AAATCTTCTCACGTCATAACCT
WF99	CTTTACTCATTTTTTCTACCGGTACATCCATGACATTCTATAACTTGATA
WF129	CCCGGCGTGTCAATAATATC

Supplementary Note 1: Specificity of roGFP1_R12 for the glutathione couple.

The interpretation of the physiological significance of the redox potential reported by the roGFP1_R12 probe requires understanding with which cellular redox couples it can interact *in vivo*. In this note, we (a) present the evidence for the specificity of roGFP1_R12 for the glutathione couple (b) discuss the performance of the sensor we used relative to that of the glutaredoxin-coupled sensor grx1-roGFP2, and (c) discuss our rationale for choosing roGFP1_R12 rather than grx1-roGFP2 to probe *in vivo* redox biology in *C. elegans*.

(a) *In vitro*, *in vivo* and structural evidence for roGFP specificity
Andreas Meyer's group performed several experiments *in vitro* demonstrating that the oxidation of the related sensors roGFP1 and roGFP2 is controlled specifically by the glutathione couple in a manner catalyzed by glutaredoxin[4, 5, 6]. They showed *in vitro* that oxidized roGFP: (i) does not react with NADPH or ascorbate; (ii) is not reduced by recombinant poplar thioredoxin h3 (in conjunction with NADPH and NADPH-dependent thioredoxin reductase) or by protein disulfide isomerase; (iii) reacts very slowly with glutathione; and (iv) reacts very quickly with glutathione upon addition of *Arabidopsis thaliana* glutaredoxin ($t_{1/2} \sim 2$ minutes). Jakob Winther's group developed a structurally similar rxYPF sensor which shows similar properties to roGFP *in vitro*: it does not interact with thioredoxin *in vivo* or *in vitro*, and is reduced by glutathione *in vitro* and *in vivo* only in the presence of glutaredoxin[7].

Tobias Dick's group unsuccessfully tried to build an roGFP2-based sensor responsive to the thioredoxin couple by coupling roGFP2 to human thioredoxin[8]. Indeed, they concluded that human thioredoxin "refuses to interact with the roGFP2 intramolecular disulfide bond"[6]. The persistent lack of success in building an roGFP based sensor specific to the thioredoxin couple lead Meyer and Dick to model whether this sensor's specificity could be the result of differences in the structural constrains imposed by the reaction mechanisms of the glutaredoxin and thioredoxin enzymes[6]. Their careful structural modeling made them conclude that "it seems unlikely that a working Trx-roGFP redox relay can be created." On the upside, they reasoned that this strengthens the concept that roGFPs "really are highly specific probes for 2GSH/GSSG"[6].

The Winther group demonstrated *in vivo* that deletion of the two *S. cerevisiae* gluataredoxins GRX1 and GRX2 dramatically slows down the response of the rxYPF sensor[7]. This indicates that these enzymes are responsible for the fast kinetics of the sensor *in vivo*. In *Arabidopsis* there are more than 30 glutaredoxin-coding genes making a similar experiment unfeasible. The Meyer group provided evidence that the sensor responded to cytosolic glutathione by showing that in the partially GSH-deficient *Arabidopsis* mutant *cad2*, which is restricted in the activity of the first and rate limiting GSH biosynthetic enzyme glutamate-cysteine ligase, there is an increase in the roGFP2 fluorescence ratio[4]. Subsequently, the Meyer and Dick groups also found that roGFP2 is almost completely oxidized in a different *Arabidopsis* mutant with only 5% of wild-type GSH levels[6]. In their outstanding review, Meyer and Dick concluded that "taken together, studies on rxYFP and roGFP strongly support the notion that within cells these proteins communicate with the glutathione redox couple through mediation by endogenous Grxs"[6].

The spontaneous roGFP1_R12 reduction kinetics we measured *in vivo* when animals are transferred from 50 mM diamide back to normal conditions are very fast (Supplementary Fig. 1, $t_{1/2} = 4.1$ minutes); in fact, they are almost as fast as those observed *in vitro* in the presence of glutaredoxin by the Meyer and Dick groups[4, 5, 8]. Therefore, these kinetics are consistent with the presence of sufficient levels of

glutaredoxin to provide fast catalysis *in vivo*. We note that the observed rate of sensor reduction upon recovery from diamide treatment is really the composite of several rates. The oxidation of both sensor and glutathione occurs directly by diamide[9], while the reduction of the sensor requires two glutathione molecules[6, 8] and the reduction of glutathione from glutathione disulfide requires reducing equivalents provided by the $NADP^+/NADPH$ couple[10]. As a result, the observed timescale of sensor reduction upon diamide removal depends on the reduction kinetics of both sensor and glutathione. Furthermore, this timescale also depends on the rate of diamide clearance from the cytosol (when animals are shifted to plates lacking this oxidant). Thus, the equilibration between the potentials of the sensor and glutathione couples *in vivo* must occur on a faster timescale than the observed timescale of sensor reduction upon recovery from diamide treatment.

All the tissues in which we performed measurements with our sensor are known to express glutaredoxins: the pharynx and intestine express GLRX-10 and the nervous system expresses GLRX-21 (ref. [11]). However, there may be additional glutaredoxins expressed in these tissues. In *C. elegans* there are many (at least five, possibly ten) glutaredoxin-coding genes, making it unfeasible to knock out all of them. To provide additional evidence that roGFP1_R12 responds to *in vivo* changes in glutathione levels we performed an experiment essentially identical to the Meyer group's *cad2* mutant experiment (see main text and Supplementary Fig. 3), obtaining similar results.

(b) Comparison of the performance of the roGFP1_R12 and grx1-roGFP2 sensors
An roGFP-based sensor that exhibits *in vitro* fast kinetics of reduction by glutathione was developed by Tobias Dick's group by coupling of human glutaredoxin to roGFP2 (ref. [8]). In contrast to this grx1-roGFP sensor, roGFP1 and roGFP2 only become quickly reduced by glutathione *in vitro* in the presence of exogenous glutaredoxin. Thus, the coupling of grx1 to roGFP2 guarantees that the grx1-roGFP2 sensor will respond quickly to changes in the glutathione redox potential. *In vivo*, in human HeLa cells, the grx1-roGFP2 sensor responds quickly to the changes in glutathione oxidation caused by a pulse of hydrogen peroxide ($t_{1/2} \sim 10$ seconds) compared to the roGFP2 sensor ($t_{1/2} \sim 1.5$ minutes), whose response kinetics depend on endogenous grx activity[8]. This indicates that the roGFP2 sensor's response kinetics limits the ability to resolve short-lived changes in glutathione redox potential. However, when these cells are unperturbed, both sensors report stable fluorescence ratios[8] that are not statistically different from each other[6]. This indicates that both sensors are measuring the same redox potential under stable environmental conditions in HeLa cells. In unperturbed *C. elegans,* we observe that the sensor's oxidation exhibits a steady state (Supplementary Fig. 1,2), supporting the notion that both roGFP1_R12 and grx1-roGFP2 sensors should be equally good at reporting the baseline redox potential of the glutathione couple in live worms.

(c) Rationale for our choice of roGFP1_R12 over grx1-roGFP2 for *in vivo* measurements
Despite the faster kinetics of the grx1-roGFP2 sensor, we believe that the roGFP1_R12 sensor represents a better choice for our experimental needs. As we have argued above, both sensors are specific for the glutathione couple and they are both well fit for measurements under stable environmental conditions. We believe, however, that there are two important drawbacks to the grx1-coupled sensor. First, the use of this sensor inherently entails the expression at high levels of human glutaredoxin 1. At this point, we do not know whether this could result in significant changes to the normal cellular redox environment in the worm, or to changes to the physiology of the worm. Indeed, the physiological roles of the many *C. elegans* glutaredoxins are very poorly understood. We therefore believe that caution is warranted, leading us to choose the simpler sensor.

Second, in our studies of redox dynamics upon perturbation with oxidants, we were interested in having a sensor that would reflect the normal kinetics that other proteins may experience. If we had chosen to use the grx1-roGFP2 sensor, we could not have probed how quickly endogenous proteins respond to changes in the state of the glutathione pool precisely because the coupling of roGFP2 to human glutaredoxin 1 speeds up those kinetics. Because the use of roGFP1_R12 does not entail the expression of human grx1, the dynamics we measure with the roGFP1_R12 sensor are likely representative of those of many endogenous proteins (which, like roGFP1_R12, are not attached to glutaredoxins).

Supplementary Note 2: Sensitivity of protein oxidation to changes in glutathione redox potential.

In our analysis, we used a universal Nernst curve to describe the relationship between redox potential and protein oxidation for any protein undergoing reversible intramolecular disulfide bond formation or reversible bi-molecular mixed-disulfide bond formation between a cysteine and glutathione. These reactions involve the exchange of two electrons. In the unimolecular case, *i.e.* $X + 2e^- + 2H^+ \rightleftarrows XH_2$, the Nernst relation describes the reduction of an intra-molecular disulfide in a protein (including roGFP1_R12) or of a disulfide between two subunits that are part of the same protein complex. This relationship does not depend on total glutathione GSH_{tot}. In contrast, for the bimolecular half-cell reaction of the glutathione couple, *i.e.* $GS–SG + 2e^- + 2H^+ \rightleftarrows 2GSH$, the Nernst relationship does depend on GSH_{tot}. Similarly, the reduction of a protein-glutathione mixed disulfide, *i.e.* $GS–SX + 2e^- + 2H^+ \rightleftarrows GSH + HSX$, depends on the concentration of reduced glutathione, which is well approximated by GSH_{tot} when OxD_{GSH} is near zero (as is the case *in vivo*). In both instances, the resulting term involving GSH_{tot} can be absorbed into a new effective midpoint potential, $E^{\circ'} = E^{\circ'}_{GS–SX} - [RT/(2F)] \ln(GSH_{tot})$.

We note that the asymmetry in ΔOxD between negative and positive ΔE (Fig. 7b,c) comes from the fact that the slope of the Nernst curve is shallower to the left of E_i than to its right when $E_i < E^{\circ'}$ (and vice versa when $E_i > E^{\circ'}$). The maxima for positive (negative) ΔE occur when $E_i - E^{\circ'}$ is $-\Delta E/2$ ($+\Delta E/2$), because in that case ΔE extends symmetrically across the midpoint, maximizing exposure to the steepest slope. When fold-change is the relevant quantity, the appropriate sensitivity $S(E)$ of the Nernst curve is given by $(1/OxD)dOxD/dE$, or $d\log(OxD)/dE$, rather than the simple derivative $dOxD/dE$ (ref. [12]). For small ΔE the fold-change in OxD can be approximated as $\exp(S(E)\Delta E)$.

Supplementary Methods

Spatial functional data analysis
We used functional data analysis to model and analyze positional-series of E values along the A-P axis of the pharynx. E profiles were represented as functions using a B-spline basis. Smoothing was achieved by penalizing curve curvature. We used a data-driven technique, minimization of the generalized cross-validation measure (GCV), to find the optimal level of smoothing[13]. Point-wise 95% confidence intervals were calculated for each spline by adding and subtracting 1.96 standard errors to the actual fit.

Functional regression: This statistical technique is the functional equivalent of ANOVA, where functional responses are decomposed into functional effects. We used the functional linear model: $E_w(p) = \mu(p) + \alpha(p) + \beta(p) + \gamma(p) + \varepsilon_w(p)$. In this model, p is the normalized position along the anterior-posterior pharyngeal medial axis across all worms (w). The function μ represents the wild-type redox profile. The functions α and β represent departures from the wild-type redox profile in animals carrying a *daf-2* or a *daf-16* mutant allele. The function γ is an interaction term that represents the departure from the wild-type redox profile in *daf-16*; *daf-2* double mutants that is not captured by the α and β terms. The residual functions ε_w capture unaccounted variation. The ratio $\beta / (\beta + \gamma)$ represents the fraction of the total *daf-16* activity controllable by *daf-2* that is present in wild-type animals. Smoothing of the regression functions was achieved by penalizing curve curvature and optimized by the cross-validation method. Point-wise 95% confidence intervals were calculated for each regression function by adding and subtracting 1.96 standard error of the estimates of the regression function parameter vector, calculated from the covariance of the residual functions. We determined the positions where E differed among genotypes by performing a functional permutation F-test, and the positions where E differed between genotypes by performing functional permutation t-tests[13], using 10,000 permutations (data not shown).

Temporal functional data analysis
We used functional data analysis to model and analyze time-series of E values in the response to *t*-BuOOH. We first subtracted the average value of E under baseline conditions for each muscle segment. The data were represented using a B-spline basis. Smoothing was achieved by penalizing curve curvature using GCV minimization to identify the optimal level of smoothing. Point-wise 95% confidence intervals were calculated for each spline by adding and subtracting 1.96 standard errors to the actual fit.

Functional regression: We used the functional linear model: $E_{mw}(t) = \mu(t) + \alpha_m(t) + \varepsilon_{mw}(t)$, satisfying the constrain $\Sigma_m \alpha_m(t) = 0$ for all t (ref. [13]). In this model, the function μ represents the grand mean across all 64 worms (w) and three muscle segments (m), and the effect functions α_m represent departures from the grand mean specific to each of the three muscle segments. The residual functions ε_{mw} capture unaccounted variation. Smoothing of the regression functions was achieved by penalizing curve curvature and optimized by the cross-validation method. Point-wise 68.3% confidence intervals were calculated for each regression function by adding and subtracting 1 standard error of the regression function parameter-vector estimates, calculated from the covariance of the residual functions. We determined the time intervals where E differed among muscle segments by performing a functional permutation F-test, and time intervals where E differed between muscles by performing functional permutation t-tests[13], using 10,000 permutations (data not shown).

Supplementary References

1. Kimura KD, Tissenbaum HA, Liu Y, Ruvkun G. *daf-2*, an insulin receptor-like gene that regulates longevity and diapause in Caenorhabditis elegans. *Science* **277**, 942-946 (1997).

2. Patel DS*, et al.* Clustering of genetically defined allele classes in the *Caenorhabditis elegans* DAF-2 insulin/IGF-1 receptor. *Genetics* **178**, 931-946 (2008).

3. Hamer I*, et al.* An arginine to cysteine(252) mutation in insulin receptors from a patient with severe insulin resistance inhibits receptor internalisation but preserves signalling events. *Diabetologia* **45**, 657-667 (2002).

4. Meyer AJ*, et al.* Redox-sensitive GFP in Arabidopsis thaliana is a quantitative biosensor for the redox potential of the cellular glutathione redox buffer. *The Plant Journal* **52**, 973-986 (2007).

5. Schwarzlander M*, et al.* Confocal imaging of glutathione redox potential in living plant cells. *J Microsc* **231**, 299-316 (2008).

6. Meyer AJ, Dick TP. Fluorescent protein-based redox probes. *Antioxid Redox Signal* **13**, 621-650 (2010).

7. Ostergaard H, Tachibana C, Winther JR. Monitoring disulfide bond formation in the eukaryotic cytosol. *J Cell Biol* **166**, 337-345 (2004).

8. Gutscher M*, et al.* Real-time imaging of the intracellular glutathione redox potential. *Nat Methods* **5**, 553-559 (2008).

9. Dooley CT, Dore TM, Hanson GT, Jackson WC, Remington SJ, Tsien RY. Imaging dynamic redox changes in mammalian cells with green fluorescent protein indicators. *J Biol Chem* **279**, 22284-22293 (2004).

10. Gilbert HF. Molecular and cellular aspects of thiol-disulfide exchange. *Adv Enzymol Relat Areas Mol Biol* **63**, 69-172 (1990).

11. Hunt-Newbury R*, et al.* High-throughput in vivo analysis of gene expression in *Caenorhabditis elegans*. *PLoS Biol* **5**, e237 (2007).

12. Savageau MA. Parameter sensitivity as a criterion for evaluating and comparing the performance of biochemical systems. *Nature* **229**, 542-544 (1971).

13. Ramsay JO, Silverman BW. *Functional data analysis*, 2nd edn. Springer (2006).